

Experimental and numerical investigations on fracture process zone of rock–concrete interface

Dong, W.; Yang, D.; Zhou, X.; Kastiukas, G.; Zhang, B.

Published in:
Fatigue and Fracture of Engineering Materials and Structures

DOI:
[10.1111/ffe.12558](https://doi.org/10.1111/ffe.12558)

Publication date:
2017

Document Version
Author accepted manuscript

[Link to publication in ResearchOnline](#)

Citation for published version (Harvard):
Dong, W, Yang, D, Zhou, X, Kastiukas, G & Zhang, B 2017, 'Experimental and numerical investigations on fracture process zone of rock–concrete interface', *Fatigue and Fracture of Engineering Materials and Structures*, vol. 40, no. 5, pp. 820-835. <https://doi.org/10.1111/ffe.12558>

General rights

Copyright and moral rights for the publications made accessible in the public portal are retained by the authors and/or other copyright owners and it is a condition of accessing publications that users recognise and abide by the legal requirements associated with these rights.

Take down policy

If you believe that this document breaches copyright please view our takedown policy at <https://edshare.gcu.ac.uk/id/eprint/5179> for details of how to contact us.

Experimental and Numerical Investigations on Fracture Process Zone of Rock-Concrete Interface

Wei Dong^{1,*}, Dong Yang², Xiangming Zhou³, Gediminas Kastiukas⁴, Binsheng Zhang⁵

¹Associate Professor, State Key Laboratory of Coastal and Offshore Engineering, Dalian University of Technology & Ocean Engineering Joint Research Center of DUT-UWA, Dalian 116024, P. R. China

*Corresponding author: E-mail: dongwei@dlut.edu.cn

²Postgraduate student, State Key Laboratory of Coastal and Offshore Engineering, Dalian University of Technology, Dalian 116024, P. R. China. E-mail: dongyang@mail.dlut.edu.cn

³Reader, Department of Mechanical, Aerospace and Civil Engineering, Brunel University London, Uxbridge, Middlesex UB8 3PH, United Kingdom & Haitian Visiting Professor, State Key Laboratory of Coastal and Offshore Engineering, Dalian University of Technology, Dalian 116024, P. R. China. E-mail: Xiangming.Zhou@brunel.ac.uk

⁴Ph.D student, Department of Mechanical, Aerospace and Civil Engineering, Brunel University, London, UB8 3PH, United Kingdom. Email: Gediminas.Kastiukas@brunel.ac.uk

⁵Senior Lecturer, Department of Construction and Surveying, School of Engineering and Built Environment, Glasgow Caledonian University, Glasgow G4 0BA, Scotland, United Kingdom. E-mail: Ben.Zhang@gcu.ac.uk

ABSTRACT

A crack propagation criterion for a rock-concrete interface is employed to investigate the evolution of the fracture process zone (FPZ) in rock-concrete composite beams under three-point bending (TPB). According to the criterion, cracking initiates along the interface when the difference between the mode I stress intensity factor (SIF) at the crack tip caused by external loading and the one caused by the cohesive stress acting on the fictitious crack surfaces reaches the initial fracture toughness of a rock-concrete interface. From the experimental results of the composite beams with various initial crack lengths but equal depths under TPB, the interface fracture parameters are determined. In addition, the FPZ evolution in a TPB specimen is investigated by using a digital image correlation (DIC) technique. Thus, the fracture processes of the rock-concrete composite beams can be simulated by introducing the initial fracture criterion to determine the crack propagation. By comparing the load versus crack mouth opening displacement (CMOD) curves and FPZ evolution, the numerical and experimental results show a reasonable agreement, which verifies the numerical method developed in this study for analysing the crack propagation along the rock-concrete interface. Finally, based on the numerical results, the effect of ligament length on the FPZ evolution and the variations of the fracture model during crack propagation are discussed for the rock-concrete interface fracture under TPB. The results indicate that ligament length significantly affects the FPZ evolution at the rock-concrete interface under TPB, and the stress intensity factor ratio of mode II to I is influenced by the specimen size during the propagation of the interfacial crack.

Keywords: Rock-concrete interface; Interfacial fracture; FPZ evolution; Crack

45 **propagation; Numerical simulation.**

46

47 **Nomenclature**

a = crack length including cohesive crack length

A = interfacial area

A_{lig} = ligament area of the composite specimen

$CMOD$ = crack mouth opening displacement

D = depth of specimen

DIC = digital image correlation

E_i = Young's modulus

f_t = uniaxial tensile strength

f_c = uniaxial compressive strength

FPZ = fracture process zone

G_f = fracture energy of concrete

$GMTS$ = Generalised maximum tangential stress criterion

K_I^P = stress intensity factor of mode I caused by external loading

K_I^σ = of mode I caused by cohesive stress

K_{IC}^{ini} = initial stress intensity factor fracture toughness

K_{IRC}^{ini} = initial fracture toughness of rock-concrete interface

K_i = stress intensity factors

L_{FPZ}^{max} = full FPZ length

l_{FPZ} = FPZ length

$LEFM$ = linear elastic fracture mechanics

P_{ini} = initial cracking load

P_{max} = peak load

P_w = self-weight of the composite specimen

TPB = three-point bending
 W_0 = area under the load-deformation curve
 w = crack opening displacement
 w_0 = stress-free crack opening displacement
 w_s = crack opening displacement at the breaking point
 Δa = crack propagation length
 $\bar{\delta}_x$ = relative crack surface displacement in x direction
 $\bar{\delta}_y$ = relative crack surface displacement in y direction
 $\bar{\delta}_0$ = deformation when load decreases to 0
 σ = cohesive stress
 σ_s = cohesive stress at the breaking point

48

49 INTRODUCTION

50 The bonded interface between dissimilar materials, such as the interface between a
 51 concrete gravity dam and the bedrock, is always a weak link, promoting crack initiation and
 52 leading to fracture even under service loads. The linear-elastic fracture mechanics (LEFM)
 53 developed by Rice¹ has been extensively accepted as a suitable technique to analyse and
 54 evaluate the potential fracture at a bi-material interface. Based on LEFM, some interfacial
 55 fracture parameters such as fracture energy and fracture toughness were investigated
 56 through experimental and numerical studies²⁻⁴. The experimental studies indicated that the
 57 magnitude of interfacial roughness would impact the aforementioned interfacial fracture
 58 parameters, driving researchers to study its effect by investigating specimens with smooth
 59 interfaces⁵ and artificial grooving interfaces⁶. In addition, it was found that unlike
 60 homogeneous materials, the bonded interface between dissimilar materials, owing to the

mismatching material properties, is always under the combination stress state of normal and shear stresses even under the conditions of symmetric geometries and balanced external loading. Through analyzing the interfacial fracture under various combinations of shear and normal stresses^{7,8}, it was found that the fracture of the specimen along the interface always corresponded to lower mixed mode stress intensity factor (SIF) ratios. On the contrary, the cracks for higher mixed mode stress intensity factor ratios usually diverted to one side of the interface^{6,9}. In addition, the interfacial crack was inclined to kink into the weaker material when there exists a large difference in material properties between two sides of the interface¹⁰. In order to illustrate the fracture mechanism of an interface with respect to different failure modes, i.e. the crack propagates along the interface and diverts to one side of the interface, the nonlinear fracture theory, in which the strain localisation and nonlinear characteristics of the interface are taken into account, should be introduced to replace LEFM in the analysis of the interfacial fracture process.

For quasi-brittle materials, the fracture process zone (FPZ) lies in front of the crack tip, and attracts significant concerns when studying the nonlinear response of an engineering structure constructed with quasi-brittle materials during the fracture process. The effect of the FPZ on the fracture parameters of concrete, as a type of quasi-brittle material, has been extensively investigated in the last few decades. The size effect of the specific fracture energy was found to be related with the FPZ properties^{11,12}, demonstrating that the FPZ length in particular decreases rapidly when the crack propagates close to the top surface of a specimen. Consequently, the local fracture energy was found to be not constant during the whole fracture process, and instead decreased with the reduction of the FPZ length.

Combining the theoretical and experimental studies, a bilinear model on local fracture energy distribution was proposed to calculate the true specific fracture energy¹³. The significant effect of a varying FPZ on concrete fracture characteristics and the entire fracture process has engaged scientific and engineering communities. The relevant studies have been carried out through experimental investigations¹⁴⁻¹⁶ and numerical simulations^{17,18}. In addition, as one three-dimensional effect on fracture analysis, a coupled fracture mode was found to exist in cracked thick plate under shear or out-plane loading, and the intensity of the coupled mode was significantly influenced by the thickness of plate in three-dimensional finite element (FE) analysis¹⁹⁻²¹. However, the study on the evolution of the FPZ during the complete fracture process at a rock-concrete interface has been little reported. Regarding the rock-concrete interfacial fracture, it is worthwhile to point out that the derived fracture energy based on LEFM without considering the FPZ is less than that based on nonlinear fracture mechanics²² by 83% . Therefore, it is significant to incorporate the study of the FPZ evolution at the rock-concrete interface when exploring the fracture mechanism and assessing the nonlinear response of a concrete structure constructed on bedrock.

Meanwhile, the crack propagation criteria in numerical methods have been widely investigated, which demonstrate the mechanism of crack growth in quasi-brittle materials like concrete. The criterion based on the maximum principle tensile stress has been adopted to simulate fracture processes of concrete by many researchers²²⁻²⁴. In this criterion, the accuracy of the calculated stress at a crack tip is largely influenced by element meshing and computational method. Therefore, to avoid getting misleading stress values at the crack tip, the stress intensity factor (SIF) - based criteria have been employed in the analyses of

fracture processes, and gained increasing attentions in the research communities. One type of SIF-based criteria was proposed by Carpinteri and Massabó²⁵, in which the crack begins to propagate when the stress singularity at the tip of the cohesive zone vanishes, i.e. SIF is equal to 0. Later, this propagation criterion was also applied to study the crack growth in concrete²⁶, other quasi-brittle materials²⁷ and composite materials with a rock-concrete interface⁶. The other SIF-based criteria proposed by Dong²⁸ for determining the crack propagation in concrete states that a crack initiates when the difference in the SIFs at the crack tip caused by external loading and the cohesive stress reaches the initial fracture toughness of concrete. The comparison of the two SIF-based criteria in the analysis of crack propagation in concrete has been made, and the applicability of the criteria has been discussed for concrete at various strength levels²⁹. The concept of the SIF-based criterion by Dong²⁸ was also coupled with the maximum circumferential stress criterion to investigate mixed mode I-II fracture in concrete³⁰. In addition, a generalised maximum tangential stress criterion (GMTS) considering tensile stress was also employed to analyse the fracture of granite under four-point bend loading³¹. However all studies mentioned above do not pertain to specimens with blunt notches or U-notches. Considering the complex stress distribution at the notch tip under mixed mode loading, a strain energy density (SED) - based³² and crack zone model (CZM) - based³³ fracture criterion were used to predict the critical load for blunt U- and V-notched brittle specimens³⁴⁻³⁶. Meanwhile, together with the crack propagation or fracture criteria, numerical methods such as the finite element method^{28,37}, extended finite element method²⁶ and scaled boundary finite element method⁶ have been employed to simulate crack growth. These numerical methods provide an additional, effective tool to

study the FPZ evolution in both quasi-brittle materials and interfacial zones. Particularly, it is more convenient to employ numerical methods to study the size effect of the FPZ evolution which cannot be easily achieved through experimental investigations.

Therefore, the main objective of this paper is to employ a stress intensity factor (SIF) - based crack propagation criterion to investigate the FPZ evolution during the complete fracture process along a rock-concrete interface. Firstly, rock-concrete composite beams with different initial crack ratios are tested under TPB. Moreover, a DIC technique is used to investigate the FPZ evolution at the rock-concrete interface. The load versus crack mouth opening displacement (P-CMOD) curves (measured using one clip gauge mounted on the bottom surface of the specimen), crack surface opening displacement (measured through the digital image correlation technique) and the FPZ evolution based on the experimental results are compared with those from the numerical approach to verify the numerical method established in this study. Finally, the FPZ properties of composite beams with a rock-concrete interface are discussed based on the experimental and numerical results. It is expected that the experimental and numerical results presented here can lead to a better understanding of the FPZ evolution of a rock-concrete interfaces so that nonlinear fracture mechanics can be more efficiently employed to the analysis on crack propagation.

NUMERICAL METHOD

The crack propagation criterion which implements the initial fracture toughness has been adopted to successfully simulate the crack growth of mode I and mixed mode fracture in concrete^{17,28,30}. This criterion for mode I crack propagation can be described by the following formula:

$$K_I^P + K_I^\sigma = K_{IC}^{ini} \quad (1)$$

where K_I^P and K_I^σ are the mode I SIFs caused by external loading and cohesive stress, respectively, and K_{IC}^{ini} is the initial fracture toughness of concrete. In order to calculate K_I^σ , the softening traction-separation law, i.e. the tension-softening relationship, should be adopted to determine the distribution of cohesive stress on a crack surface. Meanwhile, K_{IC}^{ini} can be regarded as a material property, which represents the capability of concrete to resist crack-initiation^{38,39}. Based on the criterion, the whole fracture process of a beam under particular TPB can be described as a collection of critical crack-initiation states for a series of geometrically similar beams but with different effective crack lengths²⁸.

In the case of a rock-concrete interface, however, the crack propagation criterion mentioned above cannot be directly applied to investigate the crack growth at a rock-concrete interface. Calculating the SIFs at the crack tip for a bi-material interface is different from that for a homogeneous material. To make a distinction, the SIFs for a bi-material interface are always denoted as K_1 and K_2 instead of K_I and K_{II} in this paper. Generally, they are calculated through numerical methods, e.g. stress or displacement extrapolations. In this paper, the SIFs for a rock-concrete interface crack are calculated by the displacement extrapolation method using the ANSYS finite element code with the formulas shown as follows⁴⁰:

$$K_1 = C \lim_{r \rightarrow 0} \sqrt{\frac{2\pi}{r}} [\delta_y (\cos Q + 2\varepsilon \sin Q) + \delta_x (\sin Q - 2\varepsilon \cos Q)] \quad (2)$$

$$K_2 = C \lim_{r \rightarrow 0} \sqrt{\frac{2\pi}{r}} [\delta_y (\cos Q + 2\varepsilon \sin Q) - \delta_x (\sin Q - 2\varepsilon \cos Q)] \quad (3)$$

where

$$C = \frac{2 \cosh(\varepsilon \pi)}{(\kappa_1 + 1) / \mu_1 + (\kappa_2 + 1) / \mu_2} \quad (4)$$

$$Q = \varepsilon \ln r \quad (5)$$

$$\varepsilon = \frac{1}{2\pi} \ln \left(\frac{\frac{\kappa_1}{\mu_1} + \frac{1}{\mu_2}}{\frac{\kappa_2}{\mu_2} + \frac{1}{\mu_1}} \right) \quad (6)$$

$$\mu_i = \frac{E_i}{2(1 + \nu_i)} \quad (i = 1, 2) \quad (7)$$

$$\kappa_i = \begin{cases} (3 - \nu_i) / (1 + \nu_i) & (\text{Plain stress}) \\ (3 - 4\nu_i) & (\text{Plain strain}) \end{cases} \quad (8)$$

E_i , ν_i , δ_x and δ_y are the Young's modulus, Poisson's ratio, and the relative crack surface displacements in x and y directions, respectively.

As previously mentioned, crack growth along a rock-concrete interface is in fact a mixed mode fracture process. However, it should be noted that K_2 is far less than K_1 for a TPB beam⁴. As a consequence, the crack propagation along the rock-concrete interface in a TPB beam can be approximately considered as a mode I-dominated fracture process. Moreover, a bilinear relationship between cohesive stress (σ) and crack opening displacement (w) for a rock-concrete interface⁴¹ is adopted in the numerical method, which is shown in Fig. 1. The crack opening displacement w_s and the corresponding cohesive stress σ_s at the breaking-point of the bilinear σ - w relationship is equal to $0.8G_f/f_t$ and $0.2f_t$, respectively. The stress-free crack opening displacement w_0 equals to $6G_f/f_t$. Here, f_t and G_f are the uniaxial tensile strength and fracture energy of a rock-concrete interface, respectively. A direct tension test was conducted to measure the uniaxial tensile strength of the rock-concrete interface. 100 mm × 100 mm × 200 mm prisms were prepared, which consisted of two

189 geometrically identical blocks, i.e. rock and concrete block, respectively. The uniaxial tensile
190 strength, f_t , is calculated from the following equation:

$$191 \quad f_t = P_{\max}/A \quad (9)$$

192 where P_{\max} is the peak load, and A is the interfacial area.

193 In this paper, the crack propagation criterion is modified and extended to determine the
194 crack growth along the rock-concrete interface of a composite beam under TPB. The
195 modified crack propagation criterion for a rock-concrete interface can be expressed as
196 following:

$$197 \quad K_1^P + K_1^\sigma = K_{1RC}^{ini} \quad (10)$$

198 In Eq. (10), K_1^P and K_1^σ can be calculated by inserting the relative crack surface
199 displacements δ_x and δ_y to Eqs. (2) and (3). Thus, the initial fracture toughness of the
200 rock-concrete interface, K_{1RC}^{ini} can be calculated by deriving δ_x and δ_y with respect to the
201 initial cracking load P_{ini} . Using the crack propagation criterion, the corresponding load at any
202 certain crack length can be derived. Thus, the complete crack propagation process can be
203 simulated, in which the details of the iterative process can be referred to elsewhere²⁸.

204 **EXPERIMENTAL PROGRAM**

205 To verify the proposed crack propagation criterion, a series of composite beams with a
206 rock-concrete interface were tested under TPB to investigate the fracture process. The
207 P-CMOD curves were derived from the experimental studies. In addition, taking a composite
208 beam as an example, the FPZ evolution during the complete fracture process was also
209 studied using a DIC technique.

210 **Experimental specimens**

The geometry of the rock-concrete composite beams and the test setup are illustrated in Fig 2(a). The dimensions of the composite beams are 500 mm × 100 mm × 100 mm. Each composite beam consists of two halves, a half concrete block and a half limestone block. It should be noted that to make a composite beam, concrete was cast against the half rock block with a natural surface which was obtained after a TPB test on a pre-notched rock beam (See Fig 2(b)). The rock beams have the same dimensions as the composite ones, but with different initial crack lengths. Five series of composite beams with a_0/D from 0.2 to 0.6, denoted as TPB20 to TPB60, were prepared, and three parallel composite beams were produced for each series. Grade 42.5R Portland cement, crushed stone with the maximum size of 10 mm and medium-size river sand were used for making concrete with a mix of 1:0.62:1.81:4.20 by weight (cement : water : sand : aggregate). The composite specimens were demolded one day after casting and then cured in an environment of 23°C and 90% RH for 28 days. The material properties of rock, concrete and the interface were measured with the results presented in Table 1, in which E , ν , f_c and f_t denote the elastic modulus, Poisson's ratio, compressive strength and splitting tensile strength, respectively.

Three-point bending tests

The three-point bending tests on the rock-concrete composite beams were performed using a 250kN closed-loop servo-hydraulic testing machine (MTS) under a displacement control loading mode at a rate of 0.012 mm/min. Both the displacement at the loading point and the CMOD were measured using clip gauges. In order to measure P_{ini} , four strain gauges were symmetrically attached at the pre-notch tip on both sides of a composite beam. Strain gauges and clip gauges, together with a load cell were connected to an Integrated

Measurement & Control (IMC) dynamic data acquisition device. The setup for the TPB testing is illustrated in Fig 3.

The fracture parameters of a composite beam with a rock-concrete interface including K_{1RC}^{ini} , P-CMOD curve and G_f were derived from the results of the three-point bending tests. Based on LEFM, in order to calculate the initial fracture toughness, P_{ini} should be determined. When a crack initiates and starts to propagate, the measured strain on the two sides of the crack will suddenly and significantly decrease due to the release of fracture energy. Therefore, P_{ini} can be determined according to the variation of the measured strain at the tip of a pre-crack. Meanwhile, G_f of the rock-concrete interface was derived from the load-deformation curves, which is the same procedure to concrete suggested by RILEM⁴². The deformation at the loading point can be measured using the clip gauge mounted on the top of the specimen (See Fig. 3). G_f can be calculated from the following equation:

$$G_f = \frac{W_0 + 2P_w\delta_0}{A_{lig}} \quad (11)$$

where W_0 is the area of load-deformation curves, P_w is the self-weight of the composite specimen, δ_0 is the deformation when the load decreases to 0, and A_{lig} is the ligament area of the composite specimen.

Digital image correlation (DIC) test

In order to verify the proposed crack propagation criterion and investigate the FPZ evolution along a rock-concrete interface during the entire fracture process, the displacement on the cracking surface of beam TPB30-1 was studied using a DIC technique, with the test setup shown in Fig. 4. Before performing the TPB test, white and black spray paint was used to create a speckle pattern on one side of the potential cracking surface of a

255 TPB30-1 beam. A digital camera with a resolution of 1024×768 pixels and a host-computer
256 were used in the DIC test to measure the displacement on the crack surface. Images of the
257 deformation were snapped by the digital camera every half a second and stored in a
258 host-computer. The deformation field near the crack tip can be composed by comparing
259 images of the crack surface before and during the loading. Therefore, the complete crack
260 propagation process can be tracked using the opening and sliding displacements at the
261 rock-concrete interface obtained directly by using the DIC imaging.

262 The computational domain is selected based on the potential crack propagation route,
263 in which one analysis point was picked from every five pixels in both u and v directions (see
264 Fig. 5). For beam TPB30-1, a total of 26128 (142×184) points were picked in the
265 computational domain. The analysis lines M_iN_i ($i = 1, 2, \dots, 184$) were set for every five
266 pixels apart in the v direction, in which the u and v displacements of each analysis point can
267 be determined. In the numerical procedure, the u and v displacements of the analysis points
268 located on M_1N_1 to M_iN_i lines were determined at each load level. According to the
269 tension-softening constitutive law of a rock-concrete interface proposed by Dong⁴³, the
270 critical crack opening displacement w_0 for beam TPB30-1 equals 0.0844 mm. Thus, the FPZ
271 length and opening/sliding displacements can be determined at each load level. In addition,
272 the trajectory of crack growth can be observed through the strain-contour diagram in the
273 computational domain.

274 **EXPERIMENTAL RESULTS AND NUMERICAL VERIFICATIONS**

275 **P-CMOD curves**

276 It was observed from the experiment that the fracture of all composite beams was

caused by crack propagation along their rock-concrete interface under TPB. The experimental results, which are listed in Table 2, show that initial fracture toughness of mode II, K_{2RC}^{ini} , is much less than that of mode I, K_{1RC}^{ini} . In order to verify the proposed propagation criterion, comparisons of the experimental and numerical P-CMOD curves are made, and the results are shown in Fig. 6. Moreover, relative material properties used in numerical simulation are listed in Table 3. It can be seen that the numerical results are in a reasonably good agreement with the experimental ones, indicating the validity of the proposed crack propagation criterion in the analysis of interfacial crack propagation.

FPZ evolution

In this paper, the crack propagation process of beam TPB30-1 was studied using the DIC technique. By considering the two loading stages, i.e., $P_1 = P_{max}$ and $P_2 = 11\%P_{max}$ at the post-peak branch, i.e. the strain-softening branch, as examples, the FPZ evolution and corresponding opening/sliding displacements are illustrated in Fig. 7. Moreover, the strain fields at the two loading stages are illustrated in Fig. 8. It can be seen from Fig. 7 that the crack sliding displacement is very small compared with the crack opening displacement, which indicates that the rock-concrete interface fracture under TPB is predominantly dominated by mode I fracture.

The FPZ evolution of beam TPB30-1 is also simulated using the numerical method based on the proposed crack propagation criterion. A comparison of the crack opening displacement field is made with respect to the loading levels P_1 and P_2 between the DIC and numerical results, which are shown in Figs. 9(a) and (b). Moreover, the FPZ evolution in the complete fracture process is also analyzed, and comparisons between numerical and

299 experimental results are then made (see Fig. 10). It can be seen from Figs. 9 and 10 that the
300 numerical results are in a reasonably good agreement with the experimental ones, which
301 verifies the proposed numerical method in the analysis of FPZ evolution at a rock-concrete
302 interface.

303 **DISCUSSIONS ON FPZ EVOLUTION**

304 The experimental results obtained under the current laboratory conditions in this study
305 may to certain degree affect the expansion of the conclusions to practical engineering
306 structures due to the size effect. From the viewpoint of structure reliability assessment, it is
307 expected to have a better understanding of the size effect of FPZ evolution in quasi-brittle
308 materials and along interfaces, so that the fracture mechanism of practical structures can be
309 revealed reasonably and the failure process can be predicted precisely. In this section, the
310 verified numerical method is used to investigate the FPZ evolution at a rock-concrete
311 interface. Also the material properties used in the following numerical analyses are listed in
312 Table 3.

313 **Size effect on FPZ evolution**

314 In order to investigate the effect of a_0/D on the FPZ evolution, the fracture process of the
315 T series rock-concrete composite beams with the same size but different notch/depth (a_0/D)
316 ratios is studied using numerical analysis. The geometries of the T series composite beams
317 and the numerical results, including the initial cracking load P_{ini} , peak load P_{max} and full FPZ
318 length L_{FPZ}^{max} , are listed in Table 4. Fig. 11 shows the FPZ evolutions for the five T-series
319 composite beams. It can be seen that the FPZ length, l_{FPZ} , linearly increases until the full
320 FPZ length L_{FPZ}^{max} is reached, and then decreases rapidly for all beams. With the increase of

321 a_0/D , i.e. the decrease of ligament length, the maximum FPZ length that can be attained
322 decreases but the corresponding ratio of $\Delta a/(D - a_0)$ increases.

323 In addition, the effect of specimen size on the FPZ evolution is also studied on the L
324 series composite beams with the same a_0/D but varied sizes (see Table 5). It should be
325 noted that the whole fracture process of beams with a high depth cannot be obtained due to
326 large self-weights of the specimens. Therefore the self-weight of the L series composite
327 beams are disregarded in the numerical analyses. The FPZ evolutions of the L series beams
328 are illustrated in Fig. 12. It can be seen that the ratio of L_{FPZ}^{max} to the ligament length $(D - a_0)$
329 also gradually decreases as the depth D increases from 100 mm to 20000 mm (20 m). The
330 FPZ length begins to decrease after the FPZ fully develops in cases of small specimens, e.g.
331 Specimens L100 and L150. However, the declining tendency becomes slow with the
332 increase of specimen size. Particularly, in the cases of $D = 10$ m and 20 m, the variations of
333 the FPZ length are approximately steady as crack propagates after reaching the full FPZ.
334 The results indicate that the FPZ evolution at a rock-concrete interface is largely dependent
335 on the specimen size. Therefore, for concrete structures constructed on rock with a large
336 ligament length, the FPZ will move forward with an almost constant length, i.e. the full FPZ
337 length, under mode I-dominated fracture.

338 In order to explore the mechanism of FPZ evolution, the FPZ evolutions in the T and L
339 series specimens are illustrated together in Fig. 13, which are arranged according to the
340 ligament lengths. It can be observed that the ratio of L_{FPZ}^{max} to $(D - a_0)$ decreases as the
341 ligament length $(D - a_0)$ increases. To further verify the specimen size effect on the FPZ
342 evolution at a rock-concrete interface, the S series composite beams, which have the same

ligament length but different a_0/D ratios, are also analysed in the study. The geometries of the S series beams and numerical results are presented in Table 6. The FPZ evolutions of the S series beams are illustrated in Fig. 14. It can be seen that the FPZ length remains equal for all the S series beams even though they have different a_0/D ratios. Therefore, based on the analyses of FPZ evolution in the L, T and S series beams, it can be concluded that the ligament length indeed affects the interfacial FPZ evolution and results in the specimen size effect of FPZ (??). Meanwhile, it is also found that the ratio of L_{FPZ}^{max} to $(D - a_0)$ decreases with the increase of the ligament length $(D - a_0)$, which indicates that LEFM is appropriate for fracture analysis of structures with larger ligament length for the purpose of simplified calculation.

Effect of specimen size on K_2/K_1 ratio

Under TPB, due to the materials being different on both sides of a crack, the rock-concrete interface is under mixed mode fracture rather than under single mode fracture. Therefore, the ratio of K_2/K_1 would vary as the crack propagates along the interface. For the T series specimens, K_2/K_1 versus a/D relationships are illustrated in Fig. 15. It can be seen that these curves almost coincide with each other although they have different starting points, i.e. different a_0/D ratios. Thus, in the case of specimens with the same size, the K_2/K_1 versus a/D curve with respect to the smallest a_0/D can be regarded as the envelope of those curves for the specimens with larger a_0/D ratios. The maximum value of K_2/K_1 is 0.172, which corresponds to $a/D = 0.62$.

In addition to the effect of a_0/D , the effect of specimen size on the K_2/K_1 ratio is also studied. Fig. 16(a) illustrates the variations of K_2/K_1 for Specimens L100, L150, L200 and

365 L250, and indicates that the value of K_2/K_1 increases with the increase of specimen size.
366 However, it should be noted that, comparing with the initial K_2/K_1 corresponding to the initial
367 crack length a_0 , the increase is not significant for the maximum value of K_2/K_1 . Taking
368 Specimen L100 as an example, the initial K_2/K_1 is 0.15 and the maximum is 0.175. Therefore,
369 the initial K_2/K_1 without crack propagation can approximately reflect the maximum ratio for
370 mixed mode during the fracture process although the mode varies as the crack propagates.
371 Moreover, the value of K_2/K_1 decreases rapidly when the crack is close to the top surface of
372 a rock-concrete composite beam, leading the rock-concrete interface fracture to be mode I
373 dominated at that moment.

374 On the other hand, the effect of a_0/D on the K_2/K_1 ratio also attracts attention of
375 researchers who would measure the fracture parameters at rock-concrete interface under
376 mode I fracture. Upon this point, the LEFM analysis is conducted to investigate the effect of
377 a_0/D on the initial K_2/K_1 ratio in the initial cracking state since no crack propagation happens
378 yet. In the analysis, the external load is set as a constant value, and the initial crack length is
379 increased step by step. At each step, the corresponding K_2/K_1 at the crack tip is calculated.
380 Taking Specimen T20 as an example, the variations of K_2/K_1 during the complete fracture
381 process without considering the action of the cohesive stress are shown as the curve for
382 T20L in Fig. 15. In fact, the curve presents the variations of the initial K_2/K_1 for the
383 rock-concrete composite beams with the same size as T20 but varying a_0/D from 0.2 to 1.0.
384 It can be seen from the curve that the value of K_2/K_1 increases slowly from $a_0/D = 0.2$ until
385 the peak is reached, and then reduces completing the whole fracture process (??). The ratio
386 of K_2/K_1 reaches the peak value of 0.12 at point A when a/D is about 0.56. Fig. 16(b)

387 illustrates the variations of K_2/K_1 with respect to Specimens L100, L150, L200 and L250,
388 without considering the effect of the cohesive force. Similar to the curve for T20L in Fig. 15,
389 these curves also represent the variations of the initial K_2/K_1 for the specimens with the
390 same size as L100, L150, L200 and L250 but varying a_0/D from 0.2 to 1.0. Based on the
391 results in Fig. 16(b), it can be concluded that the initial K_2/K_1 is largely affected by the
392 specimen size. With the increase of specimen size, the initial K_2/K_1 increases for the same
393 a_0/D . Meanwhile, the value of K_2/K_1 decreases rapidly when the crack is close to the top
394 surface of the specimen, which shows a similar tendency to the variations of K_2/K_1
395 considering the effect of FPZ. Although the pure mode I fracture can be approximately
396 obtained for a TPB composite beam when a/D is close to 1, it is not convenient to conduct
397 experiment in the lab because the large pre-crack length makes a specimen break easily.
398 Therefore, it is more reasonable to test the specimens with small a_0/D and small geometry
399 size to obtain the mode I fracture at a rock-concrete interface.

400 The peak values of K_2/K_1 for different specimens with/without considering the effect of
401 FPZ are presented in Table 7. It can be seen from the table that the maximum values of
402 K_2/K_1 of all specimens are reached when a/D is around 0.57. The difference between
403 maximum K_2/K_1 value calculated with and without considering the effect of FPZ increases as
404 the beam depth increases. This can be explained by the fact that higher beams have larger
405 FPZ length so that the restriction of the cohesive stress on K_1 is more significant.

406 In order to further verify the effect of specimen size on the initial K_2/K_1 , the analyses,
407 based on LEFM, are conducted on various sizes of TPB specimens with $a_0/D = 0.3$. Fig. 17
408 illustrates the initial K_2/K_1 versus specimen depth D relationship. It can be seen from this

figure that the value of K_2/K_1 increases as the specimen depth increases, and the relationship can be approximately expressed by using a logarithmic function. Curve fitting is hence applied and the corresponding logarithmic function can be obtained as follows:

$$K_2/K_1 = 0.1 \log(D) - 0.09 \quad (12)$$

According to the results shown in Fig. 17, in the case of rock-concrete interfacial fracture, the value of K_2/K_1 is close to 0.3 for large size specimens under TPB. Combining the results in Fig. 16 indicates that the ratio of K_2/K_1 would further increase during crack propagation due to the effect of FPZ. As a consequence, in the case of a concrete dam with a crack along the interface between the concrete dam and the rock foundation, the crack may divert into the rock foundation after propagating certain length due to the increase of K_2/K_1 during the fracture process. (Why not propagate into concrete dam if concrete is weaker?)

CONCLUSIONS

A crack propagation criterion for a rock-concrete interface is proposed to investigate the FPZ evolution in rock-concrete composite beams under TPB. The experiments including the TPB testing and the DIC technique are conducted to measure the P-CMOD curves and the FPZ evolution. These results then are compared with the numerical simulations to verify the proposed criterion. Moreover, the numerical method combining with the proposed criterion is employed to study the effect of the ligament length on the FPZ evolution and the variations of fracture model during crack propagation for the rock-concrete interface fracture. The following conclusions can be drawn:

- (a) By comparing with the P-CMOD curves and the FPZ evolutions from the experimental investigations, the numerical results show a reasonably good agreement, which verifies

the proposed criterion in the analysis of rock-concrete interfacial fracture. Therefore, if the elastic moduli E of concrete and rock, the interfacial uniaxial tensile strength f_t , the interfacial fracture energy G_f and the initial fracture toughness K_{1RC}^{ini} are given, the complete fracture process at rock-concrete interface under TPB can be predicted based on the proposed numerical model.

(b) The ligament length significantly affects the FPZ evolution at a rock-concrete interface under TPB. Both experimental and numerical results show that the FPZ length linearly increases as crack propagates until the maximum FPZ length is reached, and decreases thereafter. In the case of a large ligament length, with the maximum of 14 m in this study, the decreasing tendency of the FPZ is slow and keeps an approximately plateau after its full development.

(c) The ratio of K_2/K_1 varies during the interfacial crack propagation under TPB, slowly increasing first and then decreasing. For specimens with different sizes, the maximum of K_2/K_1 can be achieved when a/D is approximate 0.57. When the crack is close the top surface of the specimen, the ratio of K_2/K_1 sharply decreases to 0, which indicates the fracture of the composite specimen is dominated by mode I failure. Specimen size affects the variations of K_2/K_1 during interfacial crack propagation. Larger K_2/K_1 ratios can be obtained for higher specimens under the same a/D . The initial K_2/K_1 ratio versus specimen depth relationship can be expressed using a logarithmic function.

ACKNOWLEDGEMENTS

The financial support of the National Natural Science Foundation of China under the grants of NSFC 51478083, NSFC 51421064 and NSFC 51109026, and the National Basic

454 Research Program of China (973 Program, Grant No. 2015CB057703) is gratefully
455 acknowledged.

456 REFERENCES

- 457 1. Rice, J. (1988) Elastic fracture mechanics concepts for interfacial cracks. *J. Appl. Mech.*
458 **55**: 98-103.
- 459 2. Bank-Sills, L., N. Travitzky, D. Ashkenazi and R. Eliasi (1999) A methodology for
460 measuring interface fracture properties of composite materials. *Int. J. Fracture*. **99**: 143-161.
- 461 3. Charalambides, P., J. Lund, A. Evans and R. McMeeking (1989) A test specimen for
462 determining the fracture resistance of bimaterial interfaces. *J. Appl. Mech.* **56**: 77-82.
- 463 4. Kishen, J. C. and V. E. Saouma (2004) Fracture of rock-concrete interfaces: laboratory
464 tests and applications. *ACI Struct. J.* **101**: 325-331.
- 465 5. Tian, H., W. Chen, D. Yang and J. Yang (2015) Experimental and numerical analysis of
466 the shear behaviour of cemented concrete-rock joints. *Rock Mech. Rock Eng.* **48**: 213-222.
- 467 6. Zhong, H., E. T. Ooi, C. Song, T. Ding, G. Lin and H. Li (2014) Experimental and numerical
468 study of the dependency of interface fracture in concrete-rock specimens on mode mixity.
469 *Eng. Fract. Mech.* **124**: 287-309.
- 470 7. Tippur, H. V. and S. Ramaswamy (1993) Measurement of mixed-mode fracture
471 parameters near cracks in homogeneous and bimaterial beams. *Int. J. Fracture*. **61**:
472 247-265.
- 473 8. Yang, S., L. Song, Z. Li and S. Huang (2008) Experimental investigation on fracture
474 toughness of interface crack for rock/concrete. *Int. J. Mod. Phys. B*. **22**: 6141-6148.
- 475 9. Slowik, V., J. C. Kishen and V. E. Saouma (1998) Mixed mode fracture of cementitious

- 476 bimaterial interfaces: Part I Experimental results. *Eng. Fract. Mech.* **60**: 83-94.
- 477 10. Porto, C., M. Parente, R. Jorge, L. Pereira and S. Griza (2016) Fracture toughness of the
478 interface between Ni-Cr/ceramic, alumina/ceramic and zirconia/ceramic systems. *Fatigue*
479 *Fract. Eng. M.* **39**: 817-829.
- 480 11. Hu, X. and K. Duan (2004) Influence of fracture process zone height on fracture energy
481 of concrete. *Cement Concrete Res.* **34**: 1321-1330.
- 482 12. Hu, X. and F. Wittmann (2000) Size effect on toughness induced by crack close to free
483 surface. *Eng. Fract. Mech.* **65**: 209-221.
- 484 13. Duan, K., X. Hu and F. Wittmann (2003) Boundary effect on concrete fracture and
485 non-constant fracture energy distribution. *Eng. Fract. Mech.* **70**: 2257-2268.
- 486 14. Otsuka, K. and H. Date (2000) Fracture process zone in concrete tension specimen. *Eng.*
487 *Fract. Mech.* **65**: 111-131.
- 488 15. Wu, Z., H. Rong, J. Zheng, F. Xu and W. Dong (2011) An experimental investigation on
489 the FPZ properties in concrete using digital image correlation technique. *Eng. Fract. Mech.*
490 **78**: 2978-2990.
- 491 16. Zhang, D. and K. Wu (1999) Fracture process zone of notched three-point-bending
492 concrete beams. *Cement Concrete Res.* **29**: 1887-1892.
- 493 17. Dong, W., X. Zhou and Z. Wu (2013) On fracture process zone and crack extension
494 resistance of concrete based on initial fracture toughness. *Constr. Build. Mater.* **49**: 352-363.
- 495 18. Liang, R. and Y.-N. Li (1991) Simulations of nonlinear fracture process zone in
496 cementitious material — a boundary element approach. *Comput. Mech.* **7**: 413-427.
- 497 19. Kotousov, A., F. Berto, P. Lazzarin and F. Pegorin (2012) Three dimensional finite

498 element mixed fracture mode under anti-plane loading of a crack. *Theor. Appl. Fract. Mec.*
499 **62**: 26-33.

500 20. Kotousov, A., P. Lazzarin, F. Berto and L. Pook (2013) Three-dimensional stress states
501 at crack tip induced by shear and anti-plane loading. *Eng. Fract. Mech.* **108**: 65-74.

502 21. Pook, L. P., A. Campagnolo, F. Berto and P. Lazzarin (2015) Coupled fracture mode of a
503 cracked plate under anti-plane loading. *Eng. Fract. Mech.* **134**: 391-403.

504 22. Červenka, J., J. C. Kishen and V. E. Saouma (1998) Mixed mode fracture of
505 cementitious bimaterial interfaces: Part II numerical simulation. *Eng. Fract. Mech.* **60**:
506 95-107.

507 23. Gerstle, W. H. and M. Xie (1992) FEM modeling of fictitious crack propagation in
508 concrete. *J. Eng. Mech.* **118**: 416-434.

509 24. Hillerborg, A., M. Modéer and P.-E. Petersson (1976) Analysis of crack formation and
510 crack growth in concrete by means of fracture mechanics and finite elements. *Cement*
511 *Concrete Res.* **6**: 773-781.

512 25. Carpinteri, A. and R. Massabó (1997) Reversal in failure scaling transition of fibrous
513 composites. *J. Eng. Mech.* **123**: 107-114.

514 26. Moës, N. and T. Belytschko (2002) Extended finite element method for cohesive crack
515 growth. *Eng. Fract. Mech.* **69**: 813-833.

516 27. Yang, Z. and A. Deeks (2007) Fully-automatic modelling of cohesive crack growth using
517 a finite element-scaled boundary finite element coupled method. *Eng. Fract. Mech.* **74**:
518 2547-2573.

519 28. Dong, W., Z. Wu and X. Zhou (2013) Calculating crack extension resistance of concrete

520 based on a new crack propagation criterion. *Constr. Build. Mater.* **38**: 879-889.

521 29. Dong, W., Z. Wu, X. Zhou and C. Wang (2016) A comparative study on two stress
522 intensity factor-based criteria for prediction of mode-I crack propagation in concrete. *Eng.*
523 *Fract. Mech.* **158**: 39-58.

524 30. Wu, Z., H. Rong, J. Zheng and W. Dong (2013) Numerical method for mixed-mode I–II
525 crack propagation in concrete. *J. Eng. Mech.* **139**.

526 31. Wang, C., Z. Zhu and H. Liu (2016) On the I–II mixed mode fracture of granite using four-
527 point bend specimen. *Fatigue Fract. Eng. M.* **Vol**: Pages (??).

528 32. Gómez, F., M. Elices, F. Berto and P. Lazzarin (2007) Local strain energy to assess the
529 static failure of U-notches in plates under mixed mode loading. *Int. J. Fracture.* **145**: 29-45.

530 33. Gómez, F., M. Elices, F. Berto and P. Lazzarin (2009) Fracture of U-notched specimens
531 under mixed mode: experimental results and numerical predictions. *Eng. Fract. Mech.* **76**:
532 236-249.

533 34. Berto, F., P. Lazzarin, F. Gómez and M. Elices (2007) Fracture assessment of U-notches
534 under mixed mode loading: two procedures based on the ‘equivalent local mode I’ concept.
535 *Int. J. Fracture.* **148**: 415-433.

536 35. Gómez, F., M. Elices, F. Berto and P. Lazzarin (2009) Fracture of V-notched specimens
537 under mixed mode (I+ II) loading in brittle materials. *Int. J. Fracture.* **159**: 121-135.

538 36. Lazzarin, P., F. Berto, M. Elices and J. Gómez (2009) Brittle failures from U- and V-
539 notches in mode I and mixed I + II mode: a synthesis based on the strain energy density
540 averaged on finite-size volumes. *Fatigue Fract. Eng. M.* **32**: 671-684.

541 37. Mu, F. and J. Vandenbossche (2016) A superimposed cohesive zone model for

542 investigating the fracture properties of concrete-asphalt interface debonding. *Fatigue Fract.*
543 *Eng. M.*

544 38. Xu, S. and H. Reinhardt (1999) Determination of double-K criterion for crack propagation
545 in quasi-brittle fracture: Part I Experimental investigation of crack propagation. *Int. J.*
546 *Fracture*. **98**: 111-149.

547 39. Xu, S. and H. Reinhardt (1999) Determination of double-K criterion for crack propagation
548 in quasi-brittle fracture: Part II Analytical evaluating and practical measuring methods for
549 three-point bending notched beams. *Int. J. Fracture*. **98**: 151-177.

550 40. Nagashima, T., Y. Omoto and S. Tani (2003) Stress intensity factor analysis of interface
551 cracks using X-FEM. *Int. J. Numer. Meth. Eng.* **56**: 1151-1173.

552 41. Dong, W., Z. Wu and X. Zhou (2016) Fracture mechanisms of rock-concrete interface:
553 experimental and numerical. *J. Eng. Mech.* 04016040.

554 42. RILEM (1985) Determination of the fracture energy of mortar and concrete by means of
555 three-point bend tests on notched beams. *Mater. Struct.* **18**: 285-290.

556 43. Dong, W., L. Zhang and Z. Wu (2014) Experiment study on tension softening constitutive
557 relation of rock-concrete interface. *J. Hydraul. Eng.* **45**: 712-719.

566 **Appendix I Tables**

567 Table 1: Mechanical properties of rock, concrete and their interface

Material	ρ (kg/m ³)	E (GPa)	ν	f_c (MPa)	f_t (MPa)
Concrete	2400	33.29	0.204	38.96	—
Rock	2668	64.39	0.198	119.2	—
Interface	—	—	—	—	1.371

568
569 Table 2: Experimental results of TPB series beams

Specimen	$S \times D \times B$ (mm×mm×mm)	a_0 (mm)	P_{ini} (kN)	P_{max} (kN)	K_{1RC}^{ini} (MPa·m ^{1/2})	K_{2RC}^{ini} (MPa·m ^{1/2})	G_f (N/m)
TPB20-1	400×100×100	20	2.322	2.644	0.332	-0.020	28.256
TPB20-2		22	2.395	2.657	0.373	-0.025	23.373
TPB20-3		22	3.467	3.725	0.539	-0.037	40.342
TPB30-1		30	1.730	2.200	0.335	-0.036	19.300
TPB30-2		31	2.094	2.385	0.412	-0.034	—
TPB30-3		30	1.326	2.068	0.254	-0.021	19.516
TPB40-1		42	1.487	1.746	0.392	-0.036	19.339
TPB40-2		40	1.741	2.162	0.434	-0.039	—
TPB50-1		50	1.154	1.409	0.385	-0.036	25.781
TPB50-2		50	0.755	1.087	0.252	-0.024	21.574
TPB50-3		51	1.075	1.493	0.371	-0.035	31.062
TPB60-1		60	0.577	0.748	0.296	-0.027	11.128

570
571 Table 3: Fracture parameters used in the numerical simulations

Specimen	K_{1RC}^{ini} (MPa·m ^{1/2})	f_t (MPa)	E (GPa)		ν		G_f (N/m)
			Concrete	Rock	Concrete	Rock	
TPB20-1	0.332	1.371	33.29	64.39	0.204	0.198	28.256
TPB30-1	0.335						19.300
TPB40-1	0.392						19.339
TPB50-1	0.385						25.781
TPB60-1	0.296						11.128
T-, L-, S-series	0.335						19.300

578 Table 4: Dimensions and numerical results of T series composite beams

Test Series	$S \times D \times B$ (mm×mm×mm)	a_0/D	P_{ini} (kN)	P_{max} (kN)	L_{FPZ}^{max} (mm)
T20	400×100×100	0.2	2.140	2.795	66.0
T30		0.3	1.640	2.160	58.0
T40		0.4	1.250	1.630	52.0
T50		0.5	0.930	1.185	44.0
T60		0.6	0.650	0.795	36.0

579

580 Table 5: Dimensions and numerical results of L series composite beams

Specimen	$S \times D \times B$ (mm×mm×mm)	a_0 (mm)	a_0/D	P_{ini} (kN)	P_{max} (kN)	L_{FPZ}^{max} (mm)
L100	400×100×100	30	0.3	1.640	2.175	58.0
L150	600×150×100	45		1.980	2.810	84.2
L200	800×200×100	60		2.230	3.325	110.0
L250	1000×250×100	75		2.430	3.755	132.0
L500	2000×500×100	150		3.380	6.270	232.0
L1000	4000×1000×100	300		5.410	9.575	392.0
L2000	8000×2000×100	600		7.850	14.320	610.0
L5000	20000×5000×100	1500		11.510	24.640	967.5
L10000	40000×10000×100	3000		16.300	36.350	1260.0
L20000	80000×20000×100	6000		20.350	52.750	1520.0

581

582 Table 6: Dimensions and numerical results of S series composite beams

Specimen	$S \times D \times B$ (mm×mm×mm)	a_0/D	$D - a_0$ (mm)	P_{ini} (kN)	P_{max} (kN)	L_{FPZ}^{max} (mm)
S1	500×125×100	0.2	100	2.400	3.240	81.2
S2	576×144×100	0.3		1.950	2.730	82.0
S3	672×168×100	0.4		1.550	2.245	82.0
S4	800×200×100	0.5		1.200	1.755	81.2
S5	1000×250×100	0.6		0.800	1.235	81.0

583

584 Table 7: Maximum values of K_2/K_1 of L series composite (??) beams

Specimen	Without cohesive force		With cohesive force		Difference of K_2/K_1 with/without cohesive force
	a/D	K_2/K_1	a/D	K_2/K_1	
L100	0.58	0.12032	0.58	0.17526	0.05494
L150	0.55	0.13783	0.55	0.20218	0.06435
L200	0.58	0.15034	0.61	0.22291	0.07257
L250	0.56	0.16026	0.56	0.23929	0.07903

585 **Appendix II Figures**

586

587

588

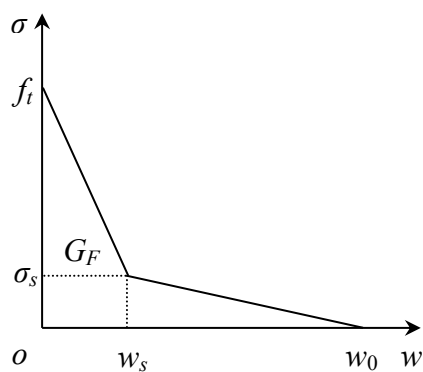
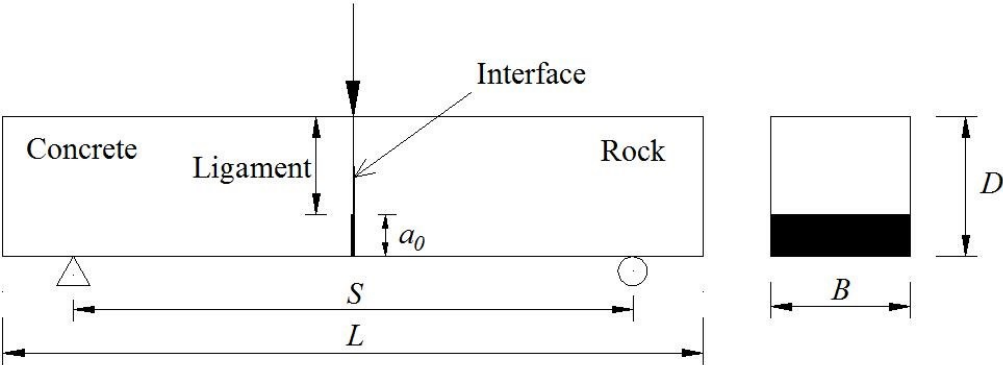


Fig.1. Bilinear stress - crack width curve for softening of concrete

589

590



(a) Specimen geometry

591

592



(b) Specimen preparation

593

Fig. 2. Geometry and preparation of rock-concrete composite specimens

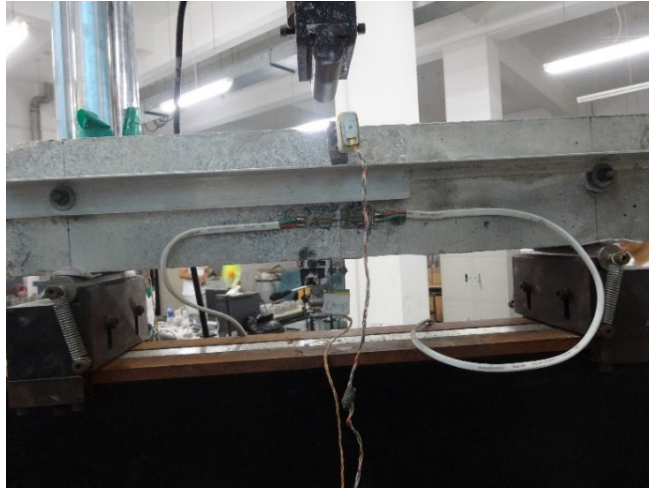


Fig. 3. Three-point bending test setup

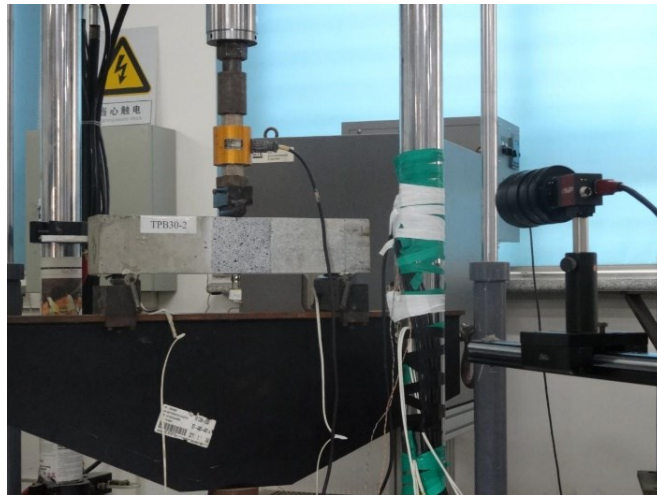


Fig. 4. DIC test setup

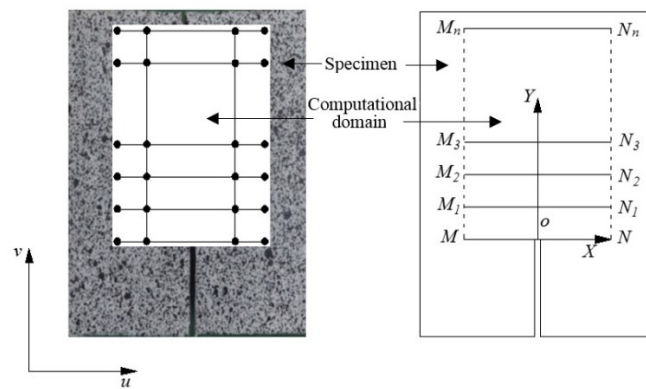
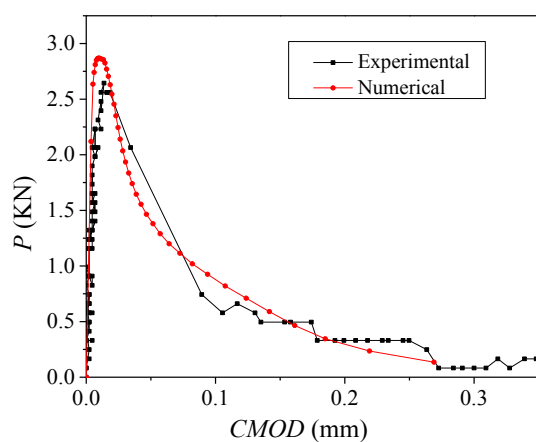
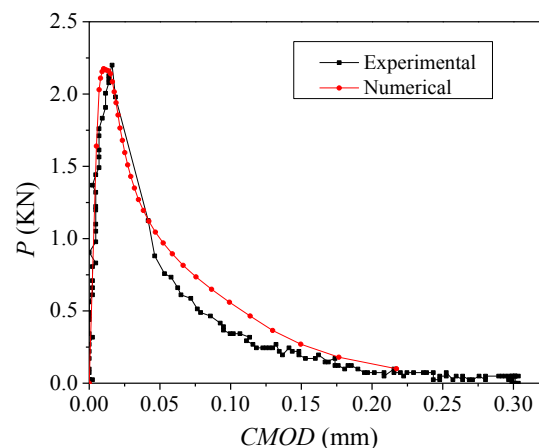


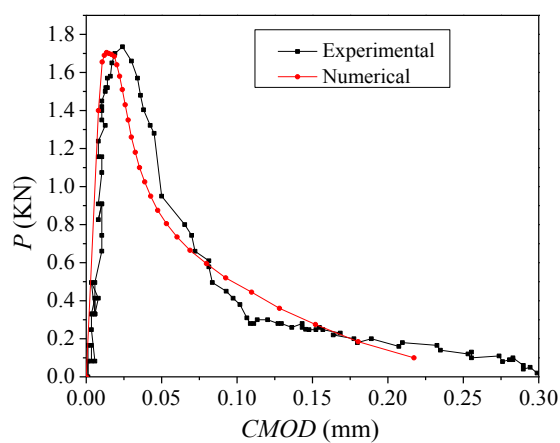
Fig. 5. Computational grids in the DIC test



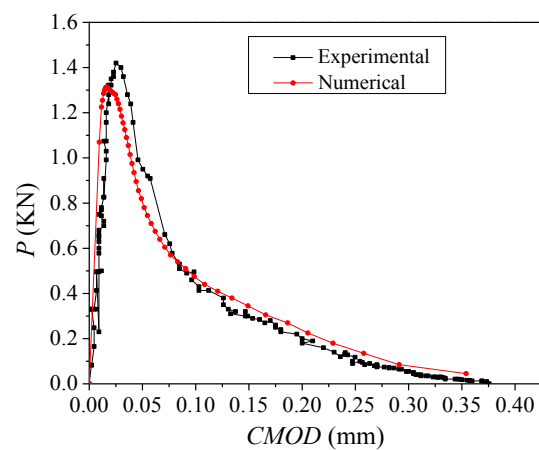
(a) TPB20-1



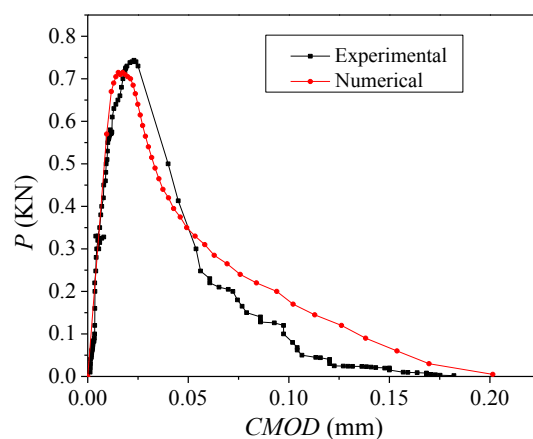
(b) TPB30-1



(c) TPB40-1

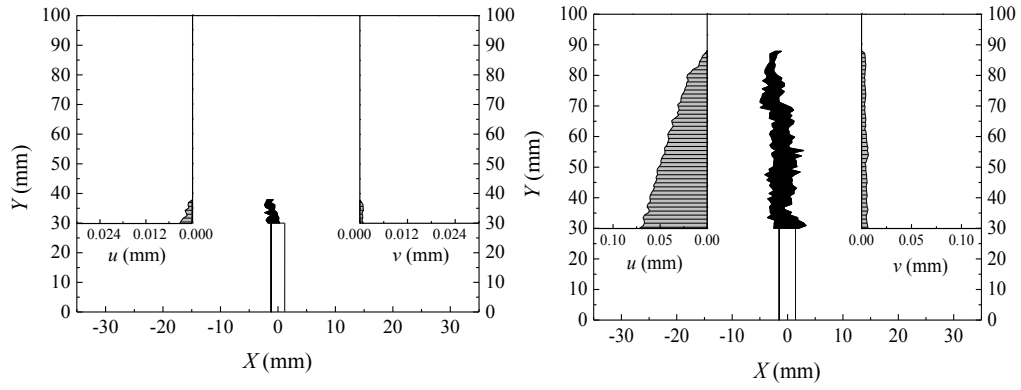


(d) TPB50-1



(e) TPB60-1

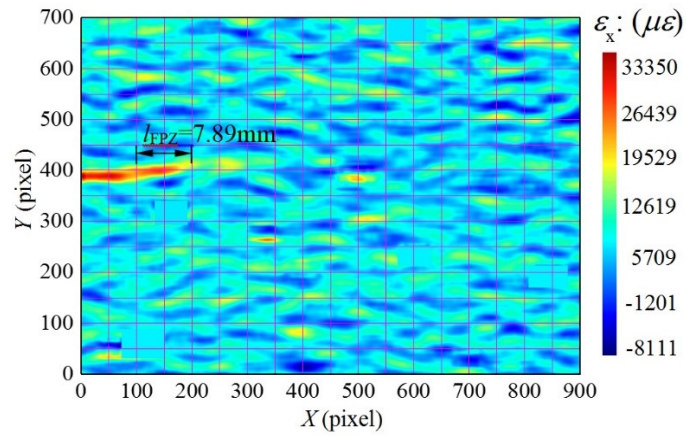
Fig. 6. Comparison of experimental and numerical P-CMOD curves (vertical axis is kN)



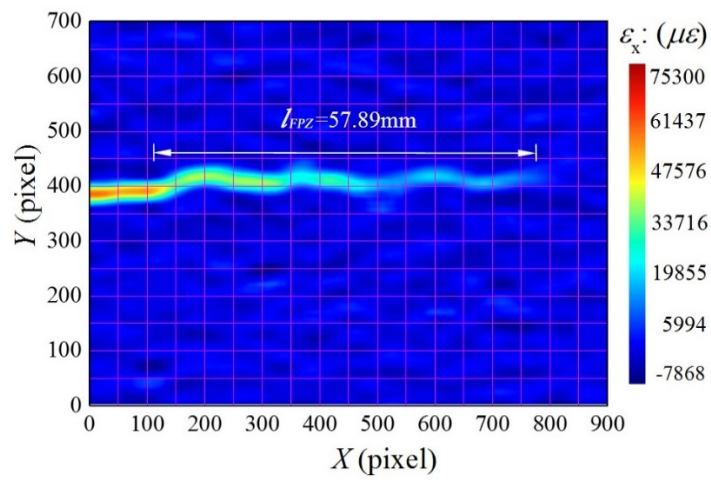
(a) Loading level P_1

(b) Loading level P_2

Fig. 7. FPZ evolution at various loading stages

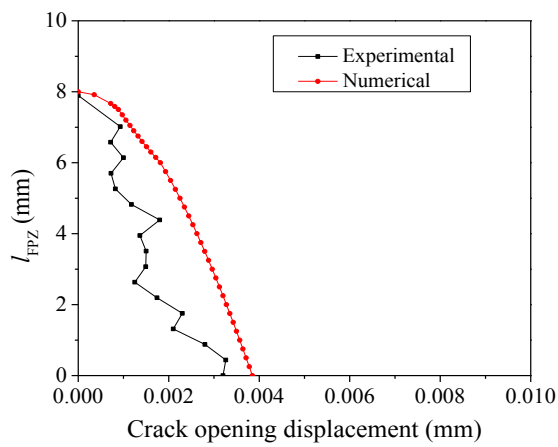


(a) Loading level P_1

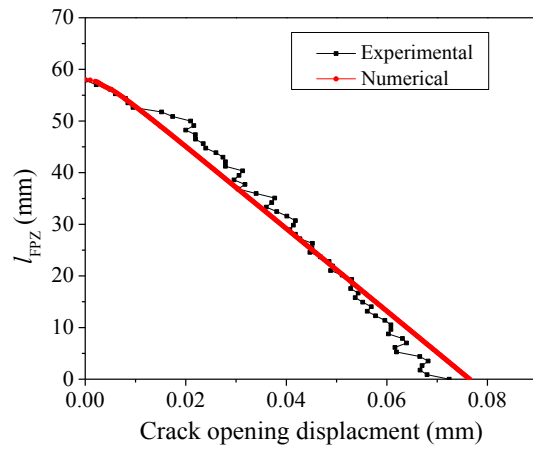


(b) Loading level P_2

Fig. 8. Strain contours at various loading stages



(a) Loading level P_1



(b) Loading level P_2

Fig. 9. Comparison of experimental and numerical crack opening displacement distributions at various loading stages

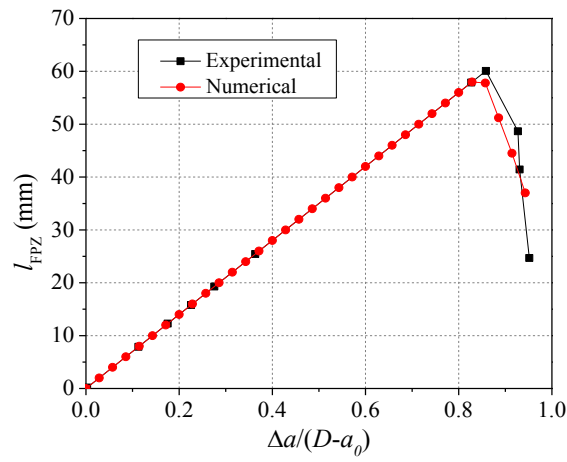


Fig. 10. Comparison of experimental and numerical FPZ evolutions for beam TPB30-1

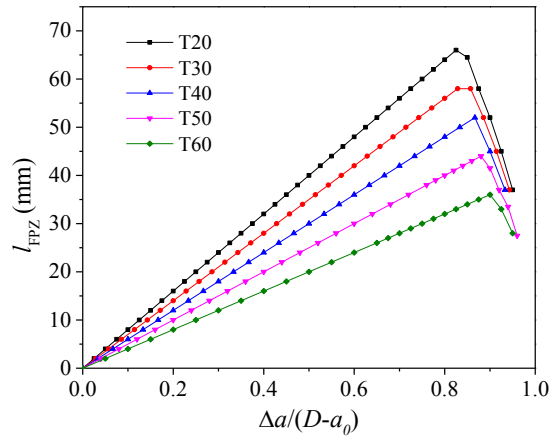


Fig. 11. Variations of FPZ length for T-series beams

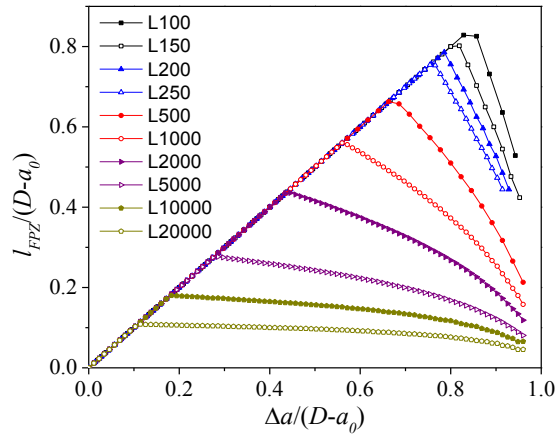


Fig. 12. Variations of FPZ length for L-series beams

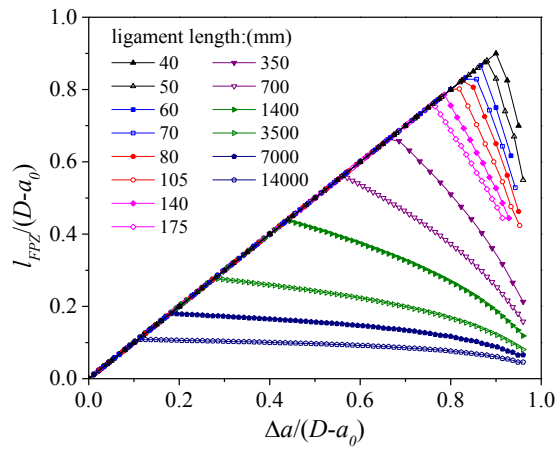


Fig. 13. FPZ evolutions for different ligament lengths

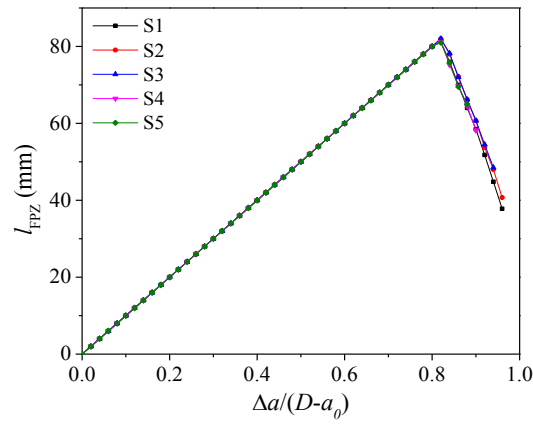


Fig. 14. Variations of fracture process zone for S-series beams

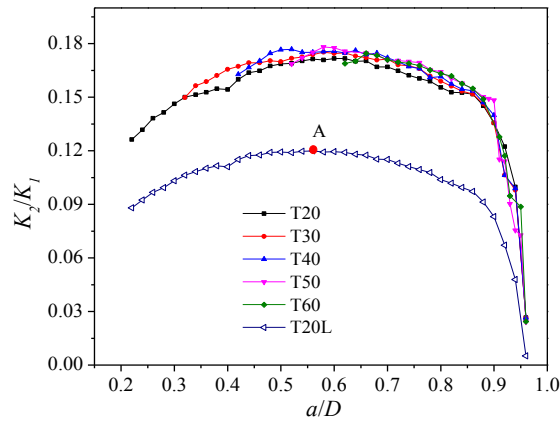
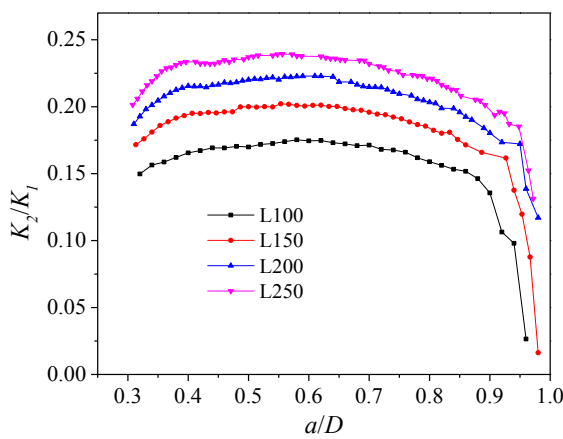
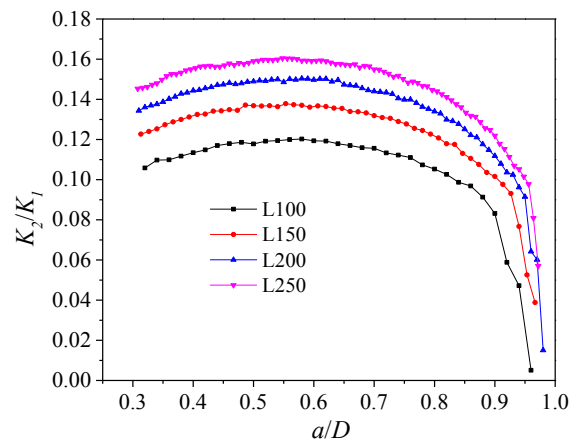


Fig. 15. K_2/K_1 variations during the complete fracture process for T-series beams and T20L



(a) With consideration of cohesive stress



(b) Without consideration of cohesive stress

Fig. 16. K_2/K_1 variations during the complete fracture process for L-series beams

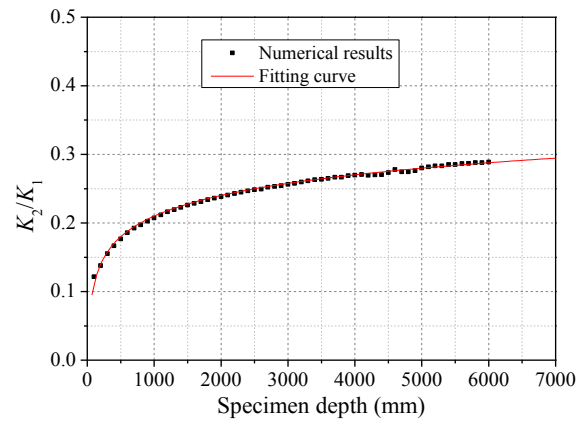


Fig. 17. K_2/K_1 versus beam depth with the fitting curve